

Selective Oxidation of a 0.1C-6Mn-2Si Third Generation Advanced High-Strength Steel During Dew-Point Controlled Annealing



MAEDEH POURMAJIDIAN and JOSEPH R. MCDERMID

The present study investigates the selective oxidation of a 0.1C-6Mn-2Si medium-Mn advanced high-strength steel during austenization annealing heat treatments as a function of process atmosphere oxygen partial pressure and annealing time. It was determined that the surface oxide growth kinetics followed a parabolic rate law with the minimum rate belonging to the lowest oxygen partial pressure atmosphere at a dew point of 223 K ($-50\text{ }^{\circ}\text{C}$). The chemistry of the surface and subsurface oxides was studied using STEM + EELS on the sample cross sections, and it was found that the surface oxides formed under the 223 K ($-50\text{ }^{\circ}\text{C}$) dew-point atmosphere consisted of a layered configuration of SiO_2 , MnSiO_3 , and MnO , while in the case of the higher p_{O_2} process atmospheres, only MnO was detected at the surface. Consistent with the Wagner calculations, it was shown that the transition to internal oxidation for Mn occurred under the 243 K ($-30\text{ }^{\circ}\text{C}$) and 278 K ($+5\text{ }^{\circ}\text{C}$) dew-point atmospheres. However, the predictions of the external to internal oxidation for Si using the Wagner model did not correlate well with the experimental findings nor did the predictions of the Maigne *et al.* model for multi-element alloys. Investigations of the internal oxide network at the grain boundaries revealed a multilayer oxide structure composed of amorphous SiO_2 and crystalline MnSiO_3 , respectively, at the oxide core and outer shell. A mechanism for the formation of the oxide morphologies observed, based on kinetic and thermodynamic factors, was proposed. It is expected that only the fine and nodule-like MnO oxides formed on the surface of the samples annealed under the 278 K ($+5\text{ }^{\circ}\text{C}$) dew-point process atmosphere for 60 and 120 seconds are sufficiently thin and of the desired dispersed morphology to promote reactive wetting by the molten galvanizing bath.

<https://doi.org/10.1007/s11661-018-4513-7>

© The Minerals, Metals & Materials Society and ASM International 2018

I. INTRODUCTION

IN recent years, medium-Mn advanced high-strength steels have garnered significant interest from the automotive industry due to their superior combination of specific strength and formability as well as their potential ability to absorb energy during crash events. Use of these alloys may allow manufacturers to design vehicles with significantly increased fuel efficiency without compromising passenger safety. However, due to the relatively short history of material development in this class of alloys, there are a limited number of studies on the other essential engineering properties of these steel grades.^[1] For example, corrosion protection of the steel

is of prime importance for maintaining the structural integrity of manufactured parts, for which the continuous galvanizing process is a cost-effective means of applying protective metallic coatings to sheet steels. In the continuous galvanizing process, a continuous steel sheet passes through an annealing heat treatment in a controlled, reducing atmosphere prior to dipping in a molten Zn(Al,Fe) bath, where the dual purpose of the annealing heat treatment is to control the microstructure of the substrate and to render the substrate surface suitable for reactive wetting by the molten alloy bath.

However, obtaining a high-quality Zn coating on the steel surface can be challenging in the case of medium-Mn substrates due to the substantial levels of alloying elements, such as Mn and Si, which are necessary for obtaining the desired mechanical properties.^[2-4] This challenge arises from the basic thermodynamics that, under typical continuous galvanizing annealing heat-treatment atmospheres, which are reducing with respect to Fe, alloying elements such as Mn, Si, Cr, and Al will be selectively oxidized. Kinetic factors, as described in a relatively simplistic manner using the

MAEDEH POURMAJIDIAN and JOSEPH R. MCDERMID are with the McMaster Steel Research Centre, McMaster University, 1280 Main Street West, Hamilton, ON L8S 4L7, Canada. Contact e-mail: mcdermid@mcmaster.ca

Manuscript submitted September 19, 2017.

Article published online March 2, 2018

Wagner model,^[5] dictate whether or not the selectively oxidized elements will manifest on the external surface and/or in the internal subsurface. In the case of the occurrence of external oxidation, it has been shown that these can prevent reactive wetting and the formation of the desired η -Fe₂Al₅Zn_x interfacial layer during dipping of the steel in the Zn(Al,Fe) bath.^[6-9] As a result, the final product can suffer from poor coating adhesion or contain unacceptable coating effects such as bare spots.

A number of authors have focused on improving the reactive wetting behavior of low-alloy, high-Si content Transformation-Induced Plasticity (TRIP) and high-Mn Twinning-Induced Plasticity (TWIP) advanced high-strength steels (AHSS) by the continuous galvanizing bath, through tailoring the annealing process atmosphere conditions^[7,10,11] as well as by modifying the alloy design.^[12-15] These contributions largely sought to determine factors resulting in the modification of the external oxides, either minimizing them through selecting process atmospheres which result in internal oxidation, embedding the oxides beneath a layer of reduced Fe from oxidation–reduction treatments or modifying the external morphology and/or chemistry to promote reactive wetting.^[10-15] Other contributions in this area have studied oxide formation from a thermodynamic standpoint^[16] and have advocated that the Si/Mn ratio be kept at 0.5 or less in order to provide a surface free of detrimental SiO₂ films which cannot be reactively wetted. However, several studies have shown that such factors as oxide morphology, surface oxide distribution, and the overall kinetics of the selective oxidation process are dominant factors in determining the ability of the galvanizing bath to reactively wet low-alloy, higher Si/Mn ratio TRIP steel surface and include such factors as the ability of surface films to be reduced by the resident-dissolved bath Al *via* aluminothermic reduction.^[17-19]

Given the plethora of studies on the reactive wetting of the low-alloy TRIP steels cited above—which commonly contain approximately 2 wt pct Mn and approximately 1.5 wt pct (Al + Si), it would be expected that medium Mn steels—with 6 wt pct Mn and slightly higher levels of Si + Al^[20,21]—would be significantly more difficult to reactively wet. However, it has been previously shown by Alibeigi *et al.*^[22] that a 5 wt pct Mn steel could be reactively wetted by a 0.20 wt pct Al (dissolved) bath provided that the intercritical annealing temperature was low enough to produce external oxides which the authors advocated could be aluminothermically reduced by the resident bath-dissolved Al. The kinetics of this process for the reduction of MnO were later quantified by Kavitha *et al.*^[19] who showed that significant external films could be reduced in practical continuous galvanizing dipping times. Furthermore, for the case of low-alloy TRIP steels, it was shown by Bellhouse *et al.*^[18] that external oxides comprising more widely dispersed nodules with thinner internodular films—which the authors theorized could be aluminothermically reduced—could be successfully reactively wetted by a 0.20 wt pct Al (dissolved) bath. In this case, the desired η -Fe₂Al₅Zn_x layer, formed by the bath reactively wetting the (then) oxide-free internodular

areas, would also precipitate on top of the remaining nodular oxides. Those authors also observed significant lift-off of the nodular oxides by fracture at the metal-oxide interface and subsequent penetration of the bath metal and η -Fe₂Al₅Zn_x formation at this interface. This general mechanism was later advocated by Sagl *et al.*^[23] for higher Mn content dual-phase (DP) steels reactively wetted by a similar Zn(Al,Fe) bath.

It has previously been shown by Bhadhon *et al.*^[24] that mechanical properties consistent with third generation AHSSs could be obtained for a 0.2C-6Mn-1.5Si-0.5Al-0.5Cr (wt pct) medium-Mn alloy intercritically annealed at the relatively low temperature of 948 K (675 °C). However, it was also shown that significantly better properties could be obtained from this steel using annealing times consistent with continuous galvanizing line processing schedules using a martensitic starting microstructure, thus requiring a 1073 K (800 °C) austenitization annealing cycle prior to intercritical annealing. This may be of some concern for later processing in the continuous galvanizing line (CGL) as the oxides produced could inhibit reactive wetting. To address this issue, the objective of this paper is to determine the selective oxidation behavior—including morphological development, chemistry, and kinetics—for a model 0.1C-6Mn-2Si prototype alloy as a function of process atmosphere oxygen partial pressure (pO₂) and annealing times ranging from 60 to 600 seconds. The selective oxidation and reactive wetting of this alloy at the intercritical temperature will be the subject of subsequent contributions. However, the results of this work will be linked qualitatively to the expected reactive wetting of this steel by the continuous galvanizing Zn(Al,Fe) bath.

II. EXPERIMENTAL

The chemical composition of the experimental medium-Mn model alloy is given in Table I. Steel sheets were received in the as cold-rolled condition with a thickness of 1.2 mm. Samples for selective oxidation heat treatments were cut from the parent material into 10 × 50 mm coupons with an abrasive water-jet cutter such that the rolling direction was parallel to the longitudinal axis of the samples. Sample preparation prior to annealing heat treatments comprised polishing the surface with 4000 grit SiC paper in order to minimize the effects of surface roughness on the selective oxidation studies. All samples were given a final clean with certified ACS reagent grade acetone (Fisher Scientific) immediately prior to annealing.

All oxidation experiments were performed using the McMaster Galvanizing Simulator (Iwatani-Surtec), for which a schematic of the corresponding thermal cycle is shown in Figure 1. The annealing cycles used comprised five isothermal holds within the range of 60 and 600 seconds at the peak annealing temperature (PAT) of 1073 K (800 °C) in an N₂-5 vol pct H₂ dew-point controlled atmosphere. The dew-point control unit (Michell Instruments) was capable of producing process atmosphere dew points ranging from 173 K (– 100 °C)

Table I. Chemical Composition of the Experimental Steel (Weight Percent)

C	Mn	Si	Al	Mo	Ti	N	S
0.106	6.241	2.023	0.040	0.072	0.011	0.003	0.003

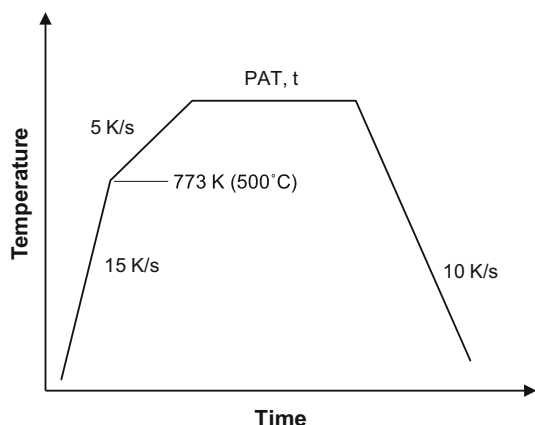


Fig. 1—Annealing heat-treatment cycle schematic.

to 293 K (+ 20 °C) with a ± 2 K accuracy. Three process atmospheres with dew points of 223 K (− 50 °C), 243 K (− 30 °C), and 278 K (+ 5 °C) were tested to explore the effect of oxygen partial pressure on the selective oxidation of Mn and Si. A detailed summary of the corresponding values of oxygen partial pressure (pO_2) for each process atmosphere along with the pH_2O/pH_2 ratios is provided in Table II. It should be noted that the values listed in Table II were derived from the FREED thermodynamic database.^[25] In the subsequent text, referrals to process atmospheres and the corresponding samples will be made by the atmosphere name per Table II. Following the PAT isothermal hold, samples were rapidly cooled to 343 K (70 °C) at a rate of − 10 K/second using N_2 gas quenching. The thermal cycle was controlled *via* a 0.5-mm-type K thermocouple welded directly to the central selective oxidation samples. All selective oxidation tests were carried out in triplicate to provide multiple samples for each of the characterization techniques used and to ensure repeatability of the experimental results. All samples were stored in anhydrous HPLC grade isopropanol after annealing in order to minimize additional oxidation prior to analysis.^[12] Further details concerning the configuration and operation of the McMaster Galvanizing Simulator are well documented and can be found elsewhere.^[26]

In order to observe the distribution and morphology of the surface oxides, annealed samples were coated with C and then examined using a JEOL 7000F field emission gun scanning electron microscope (FE-SEM) operated in secondary electron imaging mode at an acceleration voltage of 5 keV.

X-ray photoelectron spectroscopy (XPS) was performed using a PHI Quantera SXM XPS equipped with an Al $K\alpha$ X-ray source (1486.7 eV) and a hemispherical detector. The spot size was 100 μm ,

and the take-off angle was set at 45 deg. Elemental depth profiles of the steel surface were obtained by Ar ion sputtering on a 2×2 mm area with a pass energy of 140 eV and step size of 0.25 eV. All data processing was done using MultiPak 6.0 software. The obtained binding energies are accurate to within ± 0.1 eV, and all spectra were calibrated using the metallic iron binding energy of 706.62 eV. Depth measurements are considered to be accurate within ± 10 pct of the documented sputtered depth.

Transmission electron microscopy (TEM) cross sections of the samples oxidized for 600 seconds under all of the experimental process atmospheres were prepared using focused ion beam (FIB) milling with an NVision 40 by Zeiss. W and C coatings were deposited on the area of interest in order to protect the surface oxides during Ga-ion milling. The 600-second annealing time samples were used preferentially for high-resolution scanning transmission electron microscopy (HR-STEM) and electron energy loss spectroscopy (EELS) analysis because the oxides formed after the extended holding time offered a more robust configuration for chemical analysis due to the presence of coarser features yielding higher-intensity analytical signals. HR-STEM micrographs were acquired using an FEI Titan 80–300HB transmission electron microscope operated at 300 keV. Electron energy loss analyses were obtained using a Gatan Quantum GIF, where Digital Micrograph 2.3 software was used to extract elemental maps from the raw EELS data cubes.

In order to study the growth kinetics of the surface oxide layers, focused ion beam milling was also used to make two 10- μm -wide trenches perpendicular to the steel surface. Image J 1.48v software was used to measure the surface oxide thickness on tilt-corrected SEM images. Given the significant local variation in the surface oxide thickness, a minimum of 100 measurements were made per sample utilizing a grid to ensure random sampling of the external oxide layers. The average oxide thickness for the samples was reported using a 95 pct confidence interval.

III. RESULTS

Figure 2 shows SEM micrographs from the surfaces of the samples annealed at the PAT of 1073 K (800 °C) for 120, 360, and 600 seconds for all experimental process atmosphere oxygen partial pressures, as provided in Table II. These micrographs provide a visual comparison of the morphology and distribution of the oxides formed on the surface of the samples annealed under the − 50 DP, − 30 DP, and + 5 DP atmospheres. After annealing in the − 50 DP process atmosphere for 120 seconds, closely spaced oxide nodules were visible in some

Table II. Experimental Process Atmospheres Specifications at 1073 K (800 °C) Peak Annealing Temperature

Atmosphere Name	Dew Point (K)	pH ₂ O/pH ₂	pO ₂ (atm)	Holding Time (s)
– 50 DP	223	0.00125	6.87×10^{-25}	60, 120, 180, 360, 600
– 30 DP	243	0.00998	4.39×10^{-23}	60, 120, 180, 360, 600
+ 5 DP	278	0.17111	1.29×10^{-20}	60, 120, 180, 360, 600

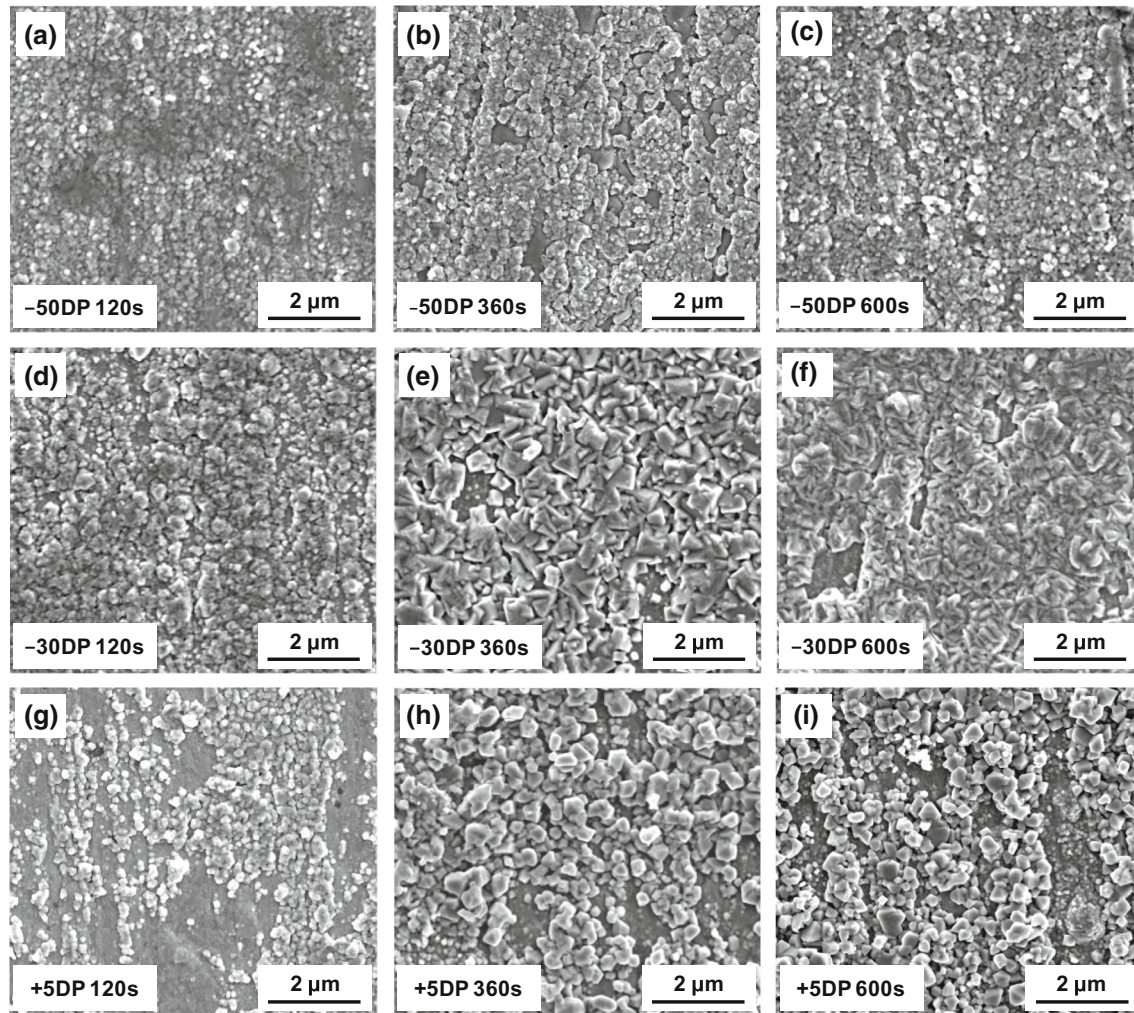


Fig. 2—Secondary electron images from sample surfaces annealed for 120, 360, and 600 s under the – 50 DP (a, b, c), – 30 DP (d, e, f), and + 5 DP (g, h, i) process atmospheres.

areas of the bulk surface, as shown in Figure 2(a), while other areas appeared to be covered by a relatively thin oxide layer. Compared to this sample, it can be seen in Figure 2(d) that a rather uniform coverage by external oxide nodules resulted after the 120-second anneal for the – 30 DP process atmosphere. By increasing the oxygen partial pressure further by means of the + 5 DP process atmosphere, a significant decrease in external oxidation was observed (Figure 2(g)) such that the underlying steel substrate surface was clearly visible in some areas, likely due the oxides in these areas being very thin.

As can be seen clearly from Figures 2(b), (e), and (h), annealing at 1073 K (800 °C) for 360 seconds resulted in significant coarsening of the surface oxide nodules for all

experimental process atmospheres. Extending the holding time to 600 seconds in the case of the – 50 DP and – 30 DP samples (Figures 2(c) and (f)) resulted in surfaces that were almost entirely covered by a compact oxide layer, accompanied by further coarsening of the nodules, which was more severe in the case of the samples annealed in the – 30 DP process atmosphere. As seen from Figure 2(i), oxide coarsening was observed in the case of the + 5 DP × 600 seconds sample; however, the surface oxide nodules did not form a compact oxide layer. Furthermore, a significant fraction of the underlying substrate was visible between the oxide nodules, indicating the presence of thin oxide layers in these areas.

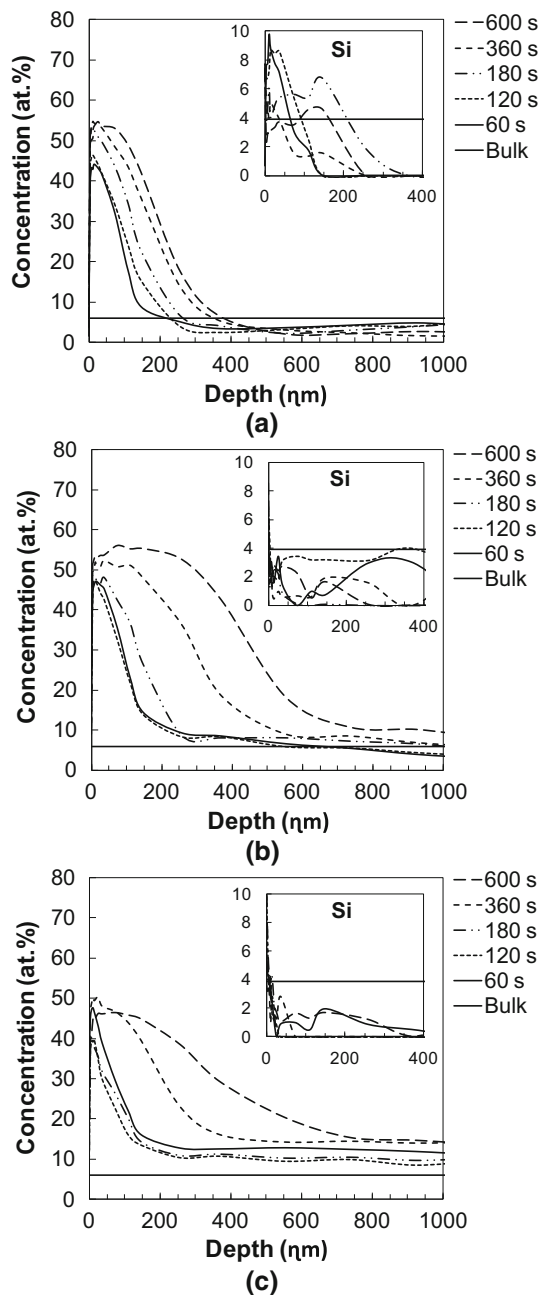


Fig. 3—Mn and Si (inset) XPS depth profiles as a function of PAT holding time for samples annealed under the (a) -50 DP, (b) -30 DP, and (c) $+5$ DP process atmospheres.

Elemental XPS depth profiles as a function of time at the PAT and process atmosphere are presented in Figure 3, where it can be seen that the surface enrichment and Mn-rich layer thickness increased with the increasing holding time at the PAT under all process atmospheres. The Mn enrichment determined for the surface of the -50 DP process atmosphere samples was slightly higher compared to that observed under the -30 DP and $+5$ DP atmospheres; however, this external oxide layer seemed to be much thinner in comparison to those of the other higher oxygen partial pressure

atmospheres. It is also worth noting that significant surface enrichment of Si was only detected for the -50 DP process atmosphere samples, as can be seen from the inset in Figure 3(a).

Further examination of Figure 3 indicates that the growth of the external oxide layer was somewhat slower for the -50 DP process atmosphere samples compared to those of the -30 DP and $+5$ DP atmospheres. Additionally, it can be seen that all the -50 DP process atmosphere Mn-depth profiles converged to the alloy bulk concentration beyond the surface Mn-enriched region (Figure 3(a)). In contrast to this, Mn concentrations higher than the bulk content were observed well below the surface-enriched region in the case of the -30 DP and $+5$ DP process atmosphere samples (Figures 3(b) and (c)), which was most pronounced in the case of the $+5$ DP \times 600 seconds sample (Figure 3(c)). This subsurface enrichment is indicative of internal oxidation, as would be expected when employing high water vapor partial pressures (*i.e.*, high p_{O_2} , Table II) in the annealing process atmosphere. However, care must be exercised in interpreting the surface oxide thickness data solely from the full-width half-maximum (FWHM) of the elemental profiles, since the increased internal oxidation depth was likely to have a contribution to the width of the XPS profiles, particularly at extended holding times and higher dew-point atmospheres. The binding energy values for O1s, Mn2p_{3/2}, and Mn2p_{1/2} peaks after a 5-nm sputter of the steel surface—*i.e.*, below the contaminated layer resulting from atmospheric exposure after removal from the MGS—were extracted from the raw XPS spectra to identify the surface oxide chemistries of the 600-second samples. An example of such an analysis is shown in Figure 4 for the -50 DP \times 600 seconds sample. From this, it can be seen that the metallic Fe peaks (binding energy 706.7 eV) appeared when several tens of nanometers of the surface oxide layers were sputtered, due to extensive coverage of the surface by the external oxides. The binding energies measured for the O1s, Mn2p_{3/2}, and Mn2p_{1/2} peaks at the surface corresponded to those of MnO, as reported by several authors^[27–29] and did not contain significant Fe oxides. A summary of these results is presented in Table III.

As mentioned earlier, direct measurements of the external oxide thicknesses were made on sample FIB cross sections for all process atmospheres and are reported as an average of at least 100 measurements over a total length of 20 μ m. Figure 5 shows a plot of external oxide thickness *vs* the square root of time, where the error bars represent the 95 pct confidence interval of the mean. The near perfect linear fit in this plot shows that the external oxide growth followed parabolic growth kinetics under all process atmospheres, as would be expected from a solid-state diffusion-controlled process.^[30,31] Furthermore, comparing the slopes of the three lines clearly indicates that the overall rate of external oxide growth under the -50 DP atmosphere was lower than that observed for the -30 DP and $+5$ DP process atmospheres. However, it should be noted that, for annealing times of less than 180 seconds, the external oxides associated with the $+5$ DP process

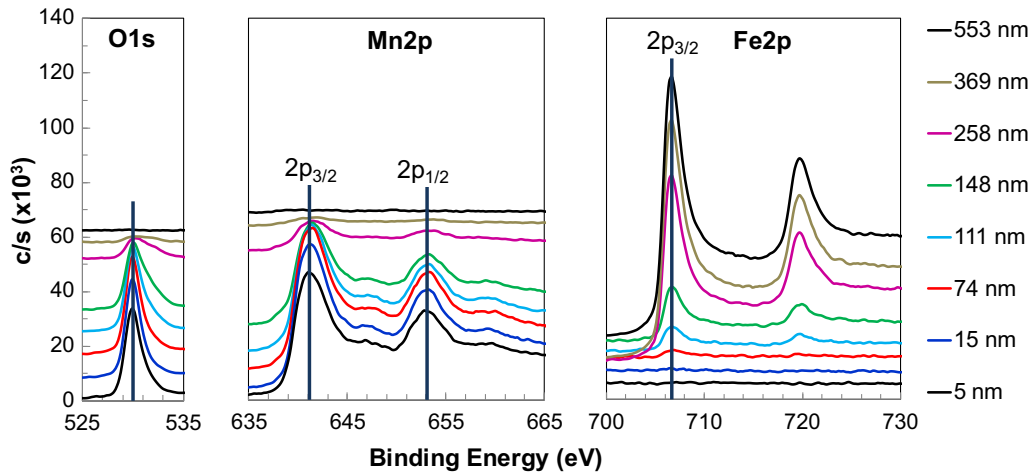


Fig. 4—XPS spectra from depth profiles of O1s, Mn2p, and Fe2p peaks for the sample annealed for 600 s under the -50 DP process atmosphere.

Table III. XPS Binding Energies of Oxides Present on the Sample Surfaces Annealed for 600 s

Atmosphere Name	Measured Binding Energies (eV)		
	O1s	Mn2p _{3/2}	Mn2p _{1/2}
- 50 DP	530.0	640.9	653.3
- 30 DP	530.3	641.4	654.1
+ 5 DP	530.2	641.1	653.6

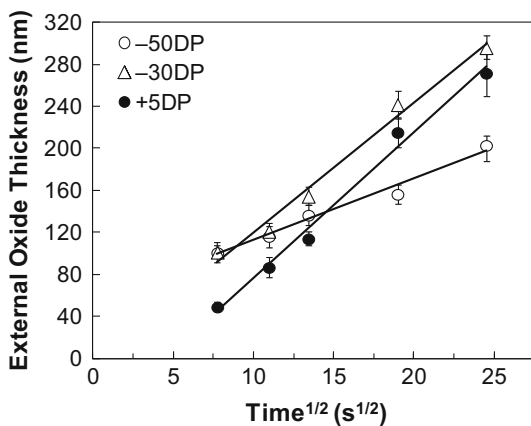


Fig. 5—Time-dependence of external oxide thickness as a function of process atmosphere dew point.

atmosphere were significantly thinner than those of the -50 DP and -30 DP process atmospheres. For example, after annealing for 60 seconds, the thinnest external oxide layer was formed under the +5 DP atmosphere (49 ± 5 nm), whereas after the 600 seconds anneal, the +5 DP process atmosphere external oxide thickness was significantly greater than that of the -50 DP atmosphere (*i.e.*, 272 ± 22 vs 203 ± 15 nm).

High-angle annular dark field (HAADF) images of the TEM cross sections of the samples annealed for 600 seconds under the -50 DP, -30 DP, and +5 DP

process atmospheres are depicted in Figure 6. The white area on top of the images is the W coating followed by a black layer representative of the C coating, both deposited prior to FIB milling to protect the external oxide structures from damage. From Figure 6(a), which shows the -50 DP sample, an external oxide layer with a nonuniform thickness can be observed. It is worth noting that, consistent with the XPS results (Figure 3(a)), no significant internal oxidation was detected for these samples, which was expected due to the relatively low pO_2 of the -50 DP atmosphere. The higher magnification image of the surface, inset of Figure 6(a), revealed three distinct layers of the external oxides, suggesting varying compositions for this constituent: first, a thin black layer a few nanometers thick (denoted as layer 3) can be seen at the steel/oxide interface; on top of this thin film, a dark gray oxide layer with varying thicknesses was observed (layer 2), and finally, light gray oxide nodules can be seen at the oxide/atmosphere interface (marked as layer 1). The latter corresponds to the oxide nodules that were visible in the SEM images as shown in Figure 2(c).

In the case of the -30 DP process atmosphere (Figure 6(b)), however, extensive internal oxidation was observed in addition to a relatively thick external oxide layer, the latter of which exhibited a polycrystalline appearance. The internal oxidation zone in this sample can be divided into two different zones with respect to the oxide morphology and distribution: the first zone comprising fine circular oxide particles within

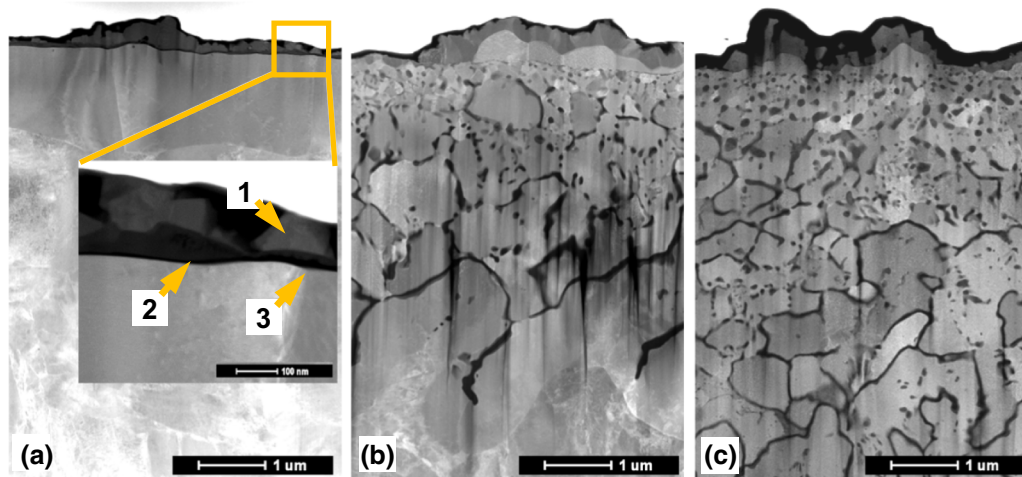


Fig. 6—HAADF images from the cross sections of the samples annealed for 600 s under the (a) – 50 DP process atmosphere, with the inset showing the external surface oxide configuration, (b) – 30 DP process atmosphere, and (c) + 5 DP process atmosphere.

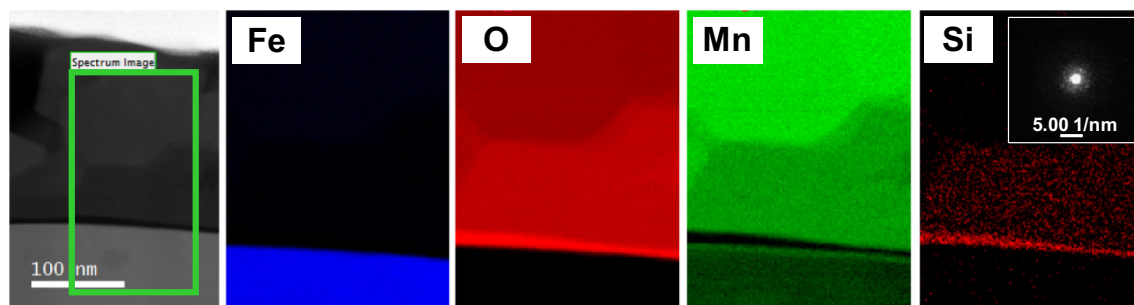


Fig. 7—HAADF image and EELS elemental maps of the external oxides on a sample annealed for 600 s under the – 50 DP process atmosphere. The inset in the Si map shows the SAD pattern acquired from the region 3 of Fig. 6(a).

the bulk microstructure along with the grain boundary oxides to a depth of approximately $0.7\ \mu\text{m}$, while beneath this region, oxides were largely present as a grain boundary network, extending to depths of approximately $4\ \mu\text{m}$ from the surface. This second zone of internal oxides appears to also decorate some subgrain boundaries. A similar morphology with a much deeper internal oxidation zone can be seen for the sample annealed under the + 5 DP process atmosphere, as shown in Figure 6(c), while in accordance with SEM results, a discontinuous, nodular external oxide configuration can be observed. It is also worth noting that, as seen in Figures 6(b) and (c), the grains close to the surfaces of the – 30 DP and + 5 DP samples appear to be much finer than those present in the bulk microstructure. This can be attributed to the pinning effect of the grain boundary oxides preventing growth of the recrystallized grains in the subsurface. It can be observed that this was not the case for the – 50 DP sample (Figure 6(a)) due to the absence of an internal oxide network. This is consistent with the work of other authors who also pointed out that this effect becomes less significant toward the inner depths of sample, due to the additional time available for grain growth prior to pinning of the grain boundaries by oxides at that depth.^[32–34]

In order to study the link between the morphology and chemistry of the oxides, selected samples were subjected to STEM + EELS analysis as these methods possess superior spatial resolution and detection limits (less than 1 at. pct) compared to XPS. Figure 7 shows the EELS elemental maps for Fe, O, Mn, and Si acquired from the external oxides of the sample annealed under the – 50 DP atmosphere for 600 seconds. The multilayer surface oxide structure of this sample hypothesized above can be observed more clearly in these images. It can be seen that the thin black layer adjacent to the steel substrate, marked as layer 3 in Figure 6(a), was an oxide enriched in Si with no significant presence of Mn. Furthermore, the selected area diffraction (SAD) pattern acquired from this layer, shown as an inset in the Si map of Figure 7, reveals that this Si-rich oxide layer was amorphous. However, for the oxide layer that was demarcated as layer 2 in Figure 6(a), the EELS maps showed an enrichment of Mn along with some Si, suggesting a Mn-Si oxide chemistry. It is worth noting that this surface Si enrichment was also detected in the Si XPS depth profiles shown in Figure 3(a). Finally, the oxide nodules at the external surface, designated as layer 1 in Figure 6(a), were identified as Mn oxide where no significant Si signal was detected in the elemental maps.

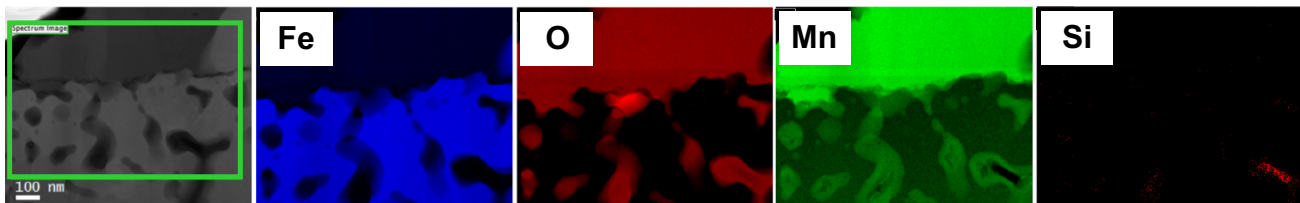


Fig. 8—HAADF image and EELS elemental maps, showing the surface and subsurface oxides of the sample annealed for 600 s under the -30 DP process atmosphere.

It is worth noting that this finding correlated well with the binding energy data presented in Table III, which determined that the top 5 nm of the oxidized steel surface, *i.e.*, layer 1 in Figure 6(a), to be MnO.

EELS elemental maps were also acquired from the internal oxide network formed as a result of annealing under the -30 DP and $+5$ DP atmospheres. Figure 8 presents the EELS elemental maps of the surface and subsurface oxides formed after annealing for 600 seconds under the -30 DP process atmosphere. It can clearly be observed that the external oxide was only composed of Mn and O with no layered oxide structure being detected at the interface, whereas the fine spherical oxides formed within the bulk and at the grain boundaries of subsurface showed occasional enrichment of Si in areas with no significant Mn being present. Further examination of the Si map in Figure 8 revealed that the Si enrichment corresponds to the core of the grain boundary oxides. This observation was also consistently found for the subsurface oxides of the $+5$ DP sample, as shown in Figure 6(c).

In the same manner, EELS elemental maps of a grain boundary oxide formed further into the subsurface from the sample annealed under the $+5$ DP atmosphere for 600 seconds are shown in Figure 9. It can be seen that, similar to the -30 DP atmosphere samples, this oxide also had a varying chemical structure, showing Si enrichment at the core of the grain boundary oxide, while suggesting the presence of a manganese silicate for the outer shell of the oxide. As discussed above, this Si-rich oxide could be identified as SiO_2 , which has been shown and is known to be present as an amorphous oxide under such conditions.^[32,35,36] This type of core-shell structure was also consistently observed in the grain boundary oxide networks formed in subsurface of the -30 DP sample.

In an effort to accurately determine the chemistries of each of the external oxide layers observed for the -50 DP sample, as per the numbered layers annotated to the STEM image in Figure 6(a), Mn, O, and Si edges of the EELS spectra of each region were extracted. The fine structures of O-K, Mn-L_{2,3}, and Si-K edges of the aforementioned EELS spectra are shown in Figure 10, where the spectra numbers correspond to the numbered layers in Figure 6(a). As can be seen from Figure 10, no Mn edge was observed in the layer 3 spectrum, while both of the O-K and Si-K edges correlated with those of SiO_2 .^[37,38] In the same manner, the shapes of the core-loss edges of O-K and Mn-L_{2,3}, along with their near-edge fine structures obtained from layer 2 in

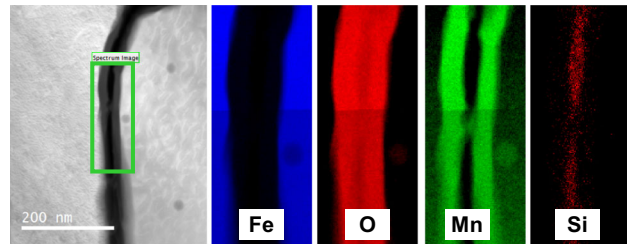


Fig. 9—HAADF image and EELS elemental maps, showing the core-shell structure of a grain boundary oxide of the sample annealed for 600 s under the $+5$ DP process atmosphere.

Figure 6(a), correspond with those reported for MnSiO_3 in the recent study of Grosvenor *et al.*^[39] Finally, the external oxide nodules were identified as MnO from the O and Mn edges^[40–43] and the fact that no Si-K edge was detected, in agreement with the XPS data reported in Table III. The same analytical procedure was carried out on the external oxides that were formed under the -30 DP and $+5$ DP atmospheres, further confirming that the external oxides in these cases comprised MnO, in agreement with the XPS binding energy analysis shown in Figure 4 and Table III. It was further found that the fine spherical internal oxides formed in the bulks of the -30 DP and $+5$ DP samples (Figure 8) correlated with the MnO spectrum in Figure 10, while the fine grain boundary oxides of the subsurface were confirmed to exhibit SiO_2 at the cores. Similar to Figure 10, inspection of the elemental edges of the EELS spectra acquired from the grain boundary oxide networks in the deeper subsurface of the -30 DP and $+5$ DP samples (Figure 9) confirmed that the oxide core consisted of amorphous SiO_2 , with the surrounding shell being identified as MnSiO_3 .

IV. DISCUSSION

In order to assist with the understanding of the internal/external transition, the classic Wagner model^[5] for the transition from internal to external oxidation was used to predict the selective oxidation modes of Mn and Si in the experimental alloy as a function of process atmosphere oxygen partial pressure ($p\text{O}_2$). Equation [1] gives the Wagner equation for the internal/external transition criterion for a binary single crystal alloy comprising a noble matrix and ignoble solute B at an absolute temperature T :

$$\left(N_B^{(o)}\right)_{crit} = \left[\frac{\pi g^* N_O^{(s)} D_O V}{2\nu D_B V_{BO\nu}} \right]^{1/2}, \quad [1]$$

where a bulk solute concentration greater than the critical mole fraction of the solute element B, $\left(N_B^{(o)}\right)_{crit}$ results in the transition from internal to external oxidation, g^* is the critical volume fraction of the precipitated oxides required to block the inward diffusion of oxygen, ν is the stoichiometric oxygen ratio for the precipitated solute oxide $BO\nu$, V is the alloy molar volume, $V_{BO\nu}$ the oxide molar volume, $N_S^{(o)}$ is the mole fraction of dissolved oxygen at the surface as per the analysis of Swisher and Turkdogan,^[44] and D_O and D_B are, respectively, the bulk diffusivities for O and the solute B in the alloy.

The values of the parameters used in Eq. [1], except those used to compute $N_O^{(s)}$, are tabulated in Table IV. It should be noted that the value of g^* most commonly used in the Wagner model is 0.3, arising from the analysis of Rapp on Ag-In alloys.^[50] However, recent experimental work by Lashgari *et al.*^[51] determined this value to be 0.2 for the case of Mn-containing steels, and

this value was used for predicting the oxidation mode of Mn in the current work; in the case of Si, however, 0.3 was employed in the calculations. More comprehensive details concerning the Wagner calculations and the equations for the terms therein, such as those used to compute $N_O^{(s)}$, are provided in Appendix A, and the process atmosphere information required for its computation is provided in Table II.

It should be noted, however, that Eq. [1] does not take into consideration either grain boundary diffusion in polycrystalline solids or the presence of multiple ignoble solutes, as is the case for the present alloy. To address these limitations, the accelerated diffusion of oxygen and alloying elements was accounted for by halving the activation energy values for bulk diffusion^[52] in Eq. [1]. In addition, the modified Wagner model proposed by Maitagne *et al.*^[52] for multicomponent systems, in which the flux of the oxidizable alloying elements toward the surface is additive and external oxidation will occur if this combined flux of the alloying elements exceeds the inward flux of O into the substrate. On this basis, the Wagner model (Eq. [1]) was modified such that external oxidation will take place if the inequality in Eq. [2] is satisfied:

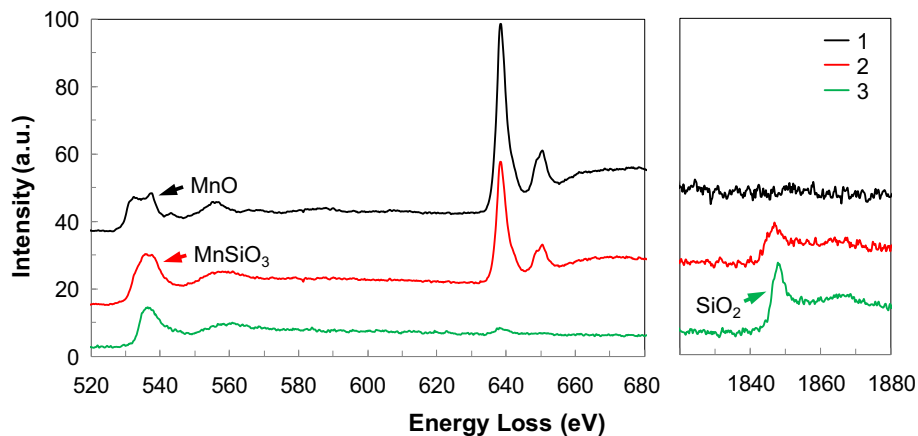


Fig. 10—O-K, Mn-L_{2,3}, and Si-K edges electron energy loss spectra acquired from the external oxides of the sample annealed for 600 s under the – 50 DP process atmosphere. The numbers correspond to different oxide regions of Fig. 6(a).

Table IV. Diffusion Data and Values for the Parameters in Eq. [1] Used for Oxidation Mode Prediction

Element or Compound in Austenite or Ferrite	D_i' (cm ² /s)	Q_i (10 ³ J/mol)	V_i (cm ³ /mol)	ν_i	References
O in γ	0.642	159.0	—	—	45
Mn in γ	0.16	261.7	—	—	46
Si in γ	0.21	242.0	—	—	45
O in α	0.037	964.0	—	—	47
Mn in α	1.49	233.5	—	—	47
Si in α	8.0	248.9	—	—	47
MnO	—	—	13.02	1	48
SiO ₂	—	—	26.12	2	48
γ -Fe	—	—	7.299	—	49
α -Fe	—	—	7.0918	—	48

Table V. Predicted Oxidation Behavior of Mn and Si for an Austenitic or Ferritic Microstructure as a Function of Process Atmosphere pO₂ at 1073 K (800 °C) Using the Wagner Equation (Eq. [1])

Atmosphere Name	Bulk Oxidation in Austenite		Bulk Oxidation in Ferrite	
	Mn	Si	Mn	Si
– 50 DP	external	external	external	external
– 30 DP	external/internal	external	external	external
+ 5 DP	internal	internal	internal	internal

$$\sum_B N_B^{(o)} [vD_B V_{BO_v}] \geq \left[\frac{g^* \pi V N_O^{(s)} D_O}{2} \right]^{1/2}, \quad [2]$$

where the left-hand side of the inequality represents the cumulative flux of ignoble solutes (in the present case, Mn and Si) to the surface and the right-hand side represents the inward flux of oxygen.

Using the treatments embodied in Eqs. [1] and [2], the oxidation modes for Mn and Si in the binary alloy (Eq.[1]) and multicomponent alloy (Eq. [2]) were computed for the process atmospheres used in the present study. Computations were conducted for both bulk and grain boundary selective oxidation. The results of the calculations for Eq. [1], *i.e.*, the binary alloy $(N_B^{(o)})_{crit}$, for both Mn and Si are compiled in Table V. In the case of grain boundary oxidation, Eq. [1] predicted external oxidation under all annealing conditions for both Mn and Si. It should be mentioned that Table V includes calculation results for both austenite and ferrite microstructures; however, it should be noted that given the annealing temperature of 1073 K (800 °C), which is significantly above the Ac₃ temperature of the experimental steel [1059 K ± 10 K (786 °C ± 10 °C)], the majority of the microstructures at the PAT likely consisted primarily of austenite and, thus, the oxidation mode was likely dominated by this phase.

The Wagner model calculation results for bulk austenite under the – 50 DP process atmosphere (Table V) are in good agreement with the XPS (Figure 3(a)) and TEM (Figure 6(a)) observations, where it can be seen that the predicted external oxidation mode for Mn and Si under the – 50 DP atmosphere was dominant. Similarly, in the case of the + 5 DP process atmosphere, the predicted internal oxidation mode for both Mn and Si was found to be consistent with the TEM (Figure 6(c)) and XPS data (Figure 3(c)), the latter of which showed the concentration profile of Mn above the bulk composition well below the substrate surface as well as the reduced surface enrichment observed. In the case of the Si XPS profiles for the + 5 DP atmosphere, the subsurface peaks (Figure 6(c)) provide some support for the occurrence of internal oxidation as these localized peaks likely resulted from either the bulk or grain boundary internal oxides.

The oxidation mode of Mn for bulk austenite under the – 30 DP process atmosphere was predicted to be borderline internal as this process atmosphere dew point

was very close to that predicted for the internal to external oxidation transition, *i.e.*, less than 1 K (Table V). It should be recalled that this prediction used the modified $g^* = 0.2$ proposed by Lashgari *et al.*^[51] The internal oxidation prediction for Mn was consistent with the XPS elemental profiles and TEM structural evidence shown in Figures 3(b), 6(b), and 8, respectively. As mentioned above, external grain boundary oxidation of the austenite was predicted to occur for both Mn and Si under the – 30 DP process atmosphere, and this is consistent with the TEM + EELS evidence presented in Figure 8 and can be said to also be consistent with the fluctuations in the Si XPS profile presented in Figure 3(b). It must, however, be pointed out that use of the classical value of $g^* = 0.3$ for Mn in Eq. [1] will also predict internal oxidation for Mn, albeit at a lower dew point of approximately 238.5 K (– 34.5 °C) and is also consistent with the above observations. Thus, no concrete conclusions can be drawn as to the preferred value for g^* for Mn in Eq. [1] from the present study.

However, in the case of Si, the predicted oxidation mode for bulk austenite was predicted to be external under the – 30 DP atmosphere and is clearly inconsistent with the experimental evidence presented in Figures 3(b), 6(b), and 8. Thus, the present form of the Wagner model or the fundamental data used for the oxidation mode prediction for Si in bulk austenite is clearly inadequate. Examination of Eq. [1] reveals that this is likely due to the value of the relative diffusivities of oxygen and silicon (*i.e.*, the $D_O/D_{B=Si}$ ratio) being approximately an order of magnitude lower than the comparable ratio for Mn, *i.e.*, 3.4×10^4 vs 4.0×10^5 , respectively. This lower relative D_O/D_B ratio for Si (*i.e.*, the higher flux of Si to the surface) was very likely the most significant factor in increasing the value of the critical mole fraction of Si for the transition to internal oxidation and the resultant increase in the predicted process atmosphere dew point for the transition from external to internal oxidation to approximately 275 K (2 °C). Thus, the overall conclusion is that the Wagner model can be used to predict the oxidation mode for Mn in the present alloy, but that the Wagner model cannot be used to accurately predict the oxidation mode transition for Si in the present Fe-0.1C-6Mn-2Si (wt pct) alloy system.

In the case of the modified multicomponent Wagner model of Maitaigne *et al.*^[52] (Eq. [2]), external oxidation of Mn and Si, both within the bulk austenite and along the austenite grain boundaries, was predicted for all

experimental process atmospheres. Further investigation of the trends predicted by this equation revealed that external oxidation was predicted for all atmospheric dew points between 173 K (−100 °C) and 373 K (+100 °C). These predictions are clearly inconsistent with the experimental results for the bulk oxidation mode of both alloying elements for the −30 DP and +5 DP process atmospheres. Thus, the additive solute oxidation effect assumed to be operative in this equation is not valid in the case of the present 6Mn + 2Si alloy.

The SEM micrographs in Figures 2(a) through (i) show that the oxidation potential of the annealing atmosphere had a significant effect on the surface oxide morphology and distribution. It was determined through XPS binding energy data (Table III) and TEM+EELS analysis (Figures 7, 8, 9, and 10) that the outermost external oxide layer comprised MnO for all process atmospheres. An increase in the isochronal surface area fraction not occupied by MnO nodules or films was determined as a result of annealing under the +5 DP atmosphere (Figures 2(g) through (i)), while the highest surface coverage by external MnO was observed under the −30 DP process atmosphere, further indicating that the oxidation potential of the process atmosphere strongly affected the oxide morphology. Furthermore, as was shown through the XPS profiles in Figure 3 and the external oxide growth rate data plotted in Figure 5, the external oxide layer formed in the −50 DP samples was significantly thinner than those formed in the other two process atmospheres for annealing times greater than 180 seconds due to its lower growth rate. However, it can also be seen from Figure 5 that the external oxide was significantly thinner for annealing times of up to 180 seconds in the case of the +5 DP process atmosphere, likely due to the effect of a stronger internal oxidation mode being operative for this process atmosphere, further supporting the above hypothesis.

The slower rate of oxide growth under the −50 DP atmosphere can be partially explained by the lower oxidation potential of this atmosphere, which in turn led to a lower adsorbed oxygen at the surface (*i.e.*, $N_O^{(s)}$, as per Eq. [A5], Appendix A) and a lower oxygen flux into the steel. Furthermore, as seen from SEM images (Figure 2(a) through (c)) and the oxidation kinetics plot in Figure 5, a relatively thick oxide layer (101 ± 9 nm) covering the steel surface was present after the 60-second hold for the −50 DP process atmosphere, meaning that further progression of the oxidation reaction was controlled by the slower outward diffusion of Mn and Si and the inward diffusion of O through the thickening surface oxide layer.^[53] Additionally, as per the TEM+EELS findings presented in Figures 6(a) and 7, respectively, the presence of a layered oxide configuration on the surface of the sample annealed under the −50 DP atmosphere further explains the slow growth rate controlled by diffusion of the oxide forming species through three different oxide layers and their corresponding interfaces, while under the −30 DP and +5 DP atmospheres, the oxidation reaction progressed through diffusion across only one interface

(Figures 6(b), (c) and 8). The surface oxides formed after the 60- and 120-second holding times under the −30 DP atmosphere were somewhat comparable to those formed under the −50 DP process atmosphere in terms of thickness and coverage; however, a significant difference between the thicknesses of the surface oxides of the two atmospheres was observed for the prolonged holding times of 360 and 600 seconds. The higher oxidation potential of the −30 DP atmosphere, *i.e.*, larger O supply, in combination with the diffusion process through a single-layer surface oxide, as described above, can be responsible for the observed increase in the oxide growth kinetics in comparison with that of the −50 DP atmosphere. The presence of more widely spaced external MnO nodules of the samples annealed under the +5 DP process atmosphere, where the internal oxidation mode was fully operative, is explained by the lower flux of solute Mn being able to reach the external oxide nucleation sites.

Thermodynamic calculations clearly show that MnO, SiO₂, MnSiO₃, and Mn₂SiO₄ form stable oxides under the annealing atmospheres used in this study.^[16] However, the morphology and formation mode (*i.e.*, internal or external) of these oxides is also dependent on kinetic factors such as the relative diffusion rates of Mn, Si, and O. Among the aforementioned oxides, SiO₂ has the highest thermodynamic stability, followed by the mixed Mn-Si oxides, with MnO being the least thermodynamically stable.^[11,54] The presence of SiO₂ as a grain boundary oxide in the subsurface of CMnSi steels has been reported by several authors at oxygen partial pressures consistent with internal oxidation.^[14,15,32,34,35,54] This can be explained by the higher thermodynamic stability of SiO₂ combined with its relatively low solubility (3.1×10^{-5} (ppm)³),^[55] and higher Si diffusivity (3.5×10^{-17} m²s^{−1}) in austenite^[55] relative to that of MnO (*i.e.*, $K_{MnO} = 7.2$ (ppm)² and $D_{Mn, \gamma} = 2.9 \times 10^{-18}$ m²s^{−1}, respectively) and the slightly lower solubility of Mn₂SiO₄ in austenite (7.6×10^{-6} (ppm)⁷, in this case assumed to be approximately the same as MnSiO₃).^[45] Thus, the likely formation sequence for these structures comprised first precipitating the more rapidly diffusing, thermodynamically stable, lower solubility SiO₂ at the grain boundaries. As Mn was able to diffuse to the grain boundaries at its lower rate, it would then react with the SiO₂ to form the observed, low solubility MnSiO₃ grain boundary phase. Further support for this hypothesis is provided in Figure 9, where it can be seen that the Mn-containing shell is slightly thinner at the bottom of the EELS map and the Si-containing core is slightly thicker, as would be expected given the diffusion-driven basis of the internal oxidation reactions. These observations are also consistent with those of other authors,^[54,56] where similar structures were observed for the internal oxidation of low Mn + Si steels. A similar mechanism would also explain the observed SiO₂ core/MnSiO₃ shell structures observed for the bulk internal oxides, as per Figure 8 and the multilayered external oxides observed in the case of the −50 DP process atmosphere (Figure 7). Having most of the Si

bound to the SiO_2 and MnSiO_3 oxides, formation of the MnO nodules at the outmost layer of the surface would be facilitated under a critically low Si/Mn ratio at the surface and continuous supply of oxygen from the atmosphere.

It has been reasonably well established that the surface oxide chemistry, morphology, distribution, and thickness can critically affect the reactive wetting of the steel substrate by the galvanizing zinc bath. A series of studies by Bellhouse and McDermid^[18,26,35] reported that reactive wetting can occur despite the presence of widely distributed, relatively thin, nodular external oxides on Al-Si TRIP-assisted steels when annealed under a low oxygen partial pressure atmosphere, whereas the more compact, thicker MnO films observed at the higher $p\text{O}_2$ were not able to be reactively wetted. Furthermore, Alibeigi *et al.*^[22] explored the reactive wetting of a 5 wt pct Mn steel by a 0.20 wt pct Al (dissolved) bath and advocated that the surface MnO layer could be aluminothermally reduced by the resident bath-dissolved Al. However, despite the large thermodynamic driving force for the aluminothermic reduction, the wetting reaction can be kinetically limited in the case of excessively thick surface of MnO layers. In a later study,^[19] it was shown that surface MnO layers thinner than 85 nm can be reduced through aluminothermic reduction during a 4-second immersion in a 0.20 Al (wt pct, dissolved) galvanizing bath.

In the present study, a variety of surface oxide chemistries and morphologies were observed under the three experimental process atmospheres. Under the -50 DP process atmosphere, a film-like multilayer oxide structure composed of SiO_2 , MnSiO_3 , and MnO was formed at the surface. It is well known that SiO_2 and manganese silicates are among the most detrimental oxides with regard to promoting the desired $\eta\text{-Fe}_2\text{Al}_5\text{Zn}_x$ interfacial layer formation. Furthermore, the -50 DP oxide layer was relatively thick (over 100 nm) for all of the experimental annealing times, making the aluminothermic reduction mechanism kinetically unfavorable.^[19] Given this factor and the unfavorable morphology, it would be expected that the surfaces of the -50 DP samples would not promote reactive wetting by the galvanizing bath. Given the similar morphology and thickness of the external MnO layer of the -30 DP process atmosphere, a similar result would be expected. Overall, it would be expected that annealing the present steel under either the -50 DP or -30 DP process atmospheres at 1073 K (800 °C) would result in poor reactive wetting by the CGL bath.

However, the surface MnO morphology and thickness were found to be significantly different as a result of increasing the oxygen partial pressure of the process atmosphere from 4.393×10^{-23} atm (*i.e.*, -30 DP, Table II) to 1.291×10^{-20} atm (*i.e.*, $+5$ DP). Under the $+5$ DP atmosphere and for the industrially relevant annealing times of 60 and 120 seconds, surface oxides with average thicknesses of 49 ± 5 and 87 ± 10 nm were formed, respectively, which were much thinner than those of the other two process atmospheres (Figure 5). Based on the kinetic model proposed by Kavitha *et al.*,^[19] these MnO layers can be

expected to be reduced in a 0.2 wt pct Al (dissolved) bath during the common CGL immersion time of approximately 4 seconds. Additionally, the very thin internodular oxide layers combined with the nodule-like oxide morphology of the $+5$ DP steels (Figures 2(g) through (i)) has been shown to favor reactive wetting mechanisms such as $\text{Fe}_2\text{Al}_5\text{Zn}_x$ formation and bridging or lift-off of the oxides by the molten zinc bath. Thus, it would be expected that the present steel annealed at 1073 K (800 °C) under the higher $p\text{O}_2 + 5$ DP process atmosphere could be successfully reactively wetted by conventional CGL baths.

V. CONCLUSIONS

It was demonstrated that process atmosphere oxygen partial pressure has strong effects on the distribution, chemistry, and oxidation mode observed during a 1073 K (800 °C) anneal of a model 0.1C-6Mn-2Si medium-Mn advanced high-strength steel. The external oxides formed under the 223 K (-50 °C) and 243 K (-30 °C) dew-point process atmospheres exhibited a film-like morphology which covered the entire steel surface, even at short holding times. For the 278 K ($+5$ °C) dew-point process atmosphere, the external oxides showed a nodular appearance with scattered distribution such that the internodular regions of the substrate surface were covered in very thin oxide films, even after a 600-second holding time. Oxide thickness measurements revealed that the surface oxide growth kinetics followed a parabolic rate law under all experimental process atmospheres, with the minimum rate belonging to the 223 K (-50 °C) dew-point process atmosphere.

XPS analysis and cross-sectional studies of the samples annealed for 600 seconds showed that, consistent with the modified Wagner model predictions for Mn, a transition from external to internal oxidation occurred under the 243 K (-30 °C) and 278 K ($+5$ °C) dew-point process atmospheres, while the Wagner model predictions for Si did not correlate with the experimental results. Moreover, the multicomponent model was incapable of predicting the oxidation mode of the experimental steel.

HR-STEM + EELS studies revealed that the external oxides formed on the steel surface under the 223 K (-50 °C) process atmosphere consisted of a layered structure of SiO_2 , MnSiO_3 , and MnO, while under the higher $p\text{O}_2$ process atmospheres, only MnO was found as the surface oxide. Similarly, it was shown that the internal network of the grain boundary oxides of the samples annealed under the 243 K (-30 °C) and 278 K ($+5$ °C) dew-point process atmospheres were composed of an amorphous SiO_2 core surrounded by an outer shell of MnSiO_3 . A mechanism for the formation of the observed oxide morphologies, based on the varying solubilities of the oxides, their relative thermodynamic stabilities, and the relative diffusion rates of Si and Mn, was described.

It is expected that the presence of film-like SiO_2 and MnSiO_3 on the surface of the 223 K (-50 °C) process atmosphere samples would result in poor reactive

wetting by the liquid metal Zn(Al,Fe) continuous galvanizing bath, and similar results are predicted in the case of the relatively thick external MnO layers formed on the samples annealed under the 243 K (− 30 °C) dew-point process atmosphere. It is expected that only the fine, nodule-like and relatively thin MnO oxides of the samples annealed under the 278 K (+ 5 °C) dew-point process atmosphere for 60 and 120 seconds will promote full reactive wetting by the molten zinc bath.

ACKNOWLEDGMENTS

This work was financially supported by the Natural Sciences and Engineering Research Council of Canada (NSERC) and Stelco Inc. through McDermid’s NSERC/Stelco Industrial Research Chair in Advanced Coated Steels. U.S. Steel Research is gratefully acknowledged for their provision of the model steels used in this study. The authors would like to thank John Thomson and Ray Fullerton at the McMaster Steel Research Centre for their technical support with the annealing simulations, Travis Casagrande and Dr. Andreas Korinek at the Canadian Centre for Electron Microscopy (CCEM) for technical and scientific assistance with TEM sample preparation and electron energy loss spectroscopy, and Dr. Li Sun of ArcelorMittal Dofasco for assistance with the XPS work.

APPENDIX A

The general equation for the diffusivity of species i is given by:

$$D_i = D_i' \exp\left(\frac{-Q_i}{RT}\right), \quad [\text{A1}]$$

where D_i' is the diffusion frequency factor of species i , Q_i is the activation energy for diffusion, and R is the universal gas constant (8.314 J/mol·K).

The mole fraction of dissolved oxygen at the surface, $N_O^{(s)}$, was provided through the analysis of Swisher and Turkdogan^[44] for the decomposition of H₂O on the steel surface to form a Henrian solution with the appropriate phase in the substrate, as per Eq. [A2]:



$$N_O^{(s)} = \frac{1}{100} \left(\frac{MW(Fe)}{MW(O)} \right) \left(\frac{p(\text{H}_2\text{O})}{p(\text{H}_2)} \right) \left(\frac{1}{K_3^i} \right) \quad [\text{A3}]$$

where $MW(Fe)$ and $MW(O)$ are the molecular weights of Fe and O, respectively; $p(\text{H}_2\text{O})$ and $p(\text{H}_2)$ are the partial pressures of water vapor and hydrogen in the process atmosphere, respectively; and K_3^i is the

equilibrium constant of reaction [A2] for phase i in the substrate (*i.e.*, austenite (γ) or ferrite (α)). These latter values are obtained from Eqs. [A4] and [A5] for austenite and ferrite, respectively^[44]:

$$\log K_3^{\gamma} = \frac{4050}{T} + 0.06 \quad [\text{A4}]$$

$$(\log K_3^{\alpha}) = \frac{5000}{T} - 0.79, \quad [\text{A5}]$$

and the $p(\text{H}_2\text{O})/p(\text{H}_2)$ ratios required for input to Eq. [A3] for the process atmospheres of interest are presented in Table II.

REFERENCES

1. D.W. Suh and S.J. Kim: *Scripta Mater.*, 2017, vol. 126, pp. 63–67.
2. M.J. Merwin: *Mater. Sci. Forum*, 2007, vol. 539, pp. 4327–32.
3. M.J. Merwin: *Iron & Steel Technol.*, 2008, vol. 5, pp. 66–84.
4. R.L. Miller: *Metall. Mater. Trans. B*, 1972, vol. 3B, pp. 905–12.
5. C. Wagner: *Zh. Elektrochem*, 1959, vol. 63, pp. 772–82.
6. T. Kato, K. Nunome, K. Kaneko, and H. Saka: *Acta Mater.*, 2000, vol. 48, pp. 2257–62.
7. J. Mahieu, S. Claessens, and B.C. De Cooman: *Metall. Mater. Trans. A*, 2001, vol. 32A, pp. 2905–08.
8. J. Maki, J. Mahieu, B.C. De Cooman, and S. Claessens: *Mater. Sci. Technol.*, 2003, vol. 19, pp. 125–31.
9. J. Mahieu, B.C. De Cooman, J. Maki, and S. Claessens: *Iron Steelmak.*, 2002, vol. 29, pp. 29–34.
10. M. Blumenau, M. Norden, F. Friedel, and K. Peters: *Surf. Coat. Technol.*, 2011, vol. 206, pp. 559–67.
11. L. Cho, S.J. Lee, M.S. Kim, Y.H. Kim, and B.C. De Cooman: *Metall. Mater. Trans. A*, 2014, vol. 45A, pp. 5158–72.
12. E.M. Bellhouse, A. Mertens, and J.R. McDermid: *Mater. Sci. Eng., A*, 2007, vol. 463, pp. 147–56.
13. L. Cho, M.S. Kim, Y.H. Kim, and B.C. De Cooman: *Metall. Mater. Trans. A*, 2014, vol. 45A, pp. 4484–98.
14. L. Cho, E.J. Seo, G.S. Jung, D.W. Suh, and B.C. De Cooman: *Metall. Mater. Trans. A*, 2016, vol. 47A, pp. 1705–19.
15. J. Oh, L. Cho, M. Kim, K. Kang, and B.C. De Cooman: *Metall. Mater. Trans. A*, 2016, vol. 47A, pp. 5474–86.
16. Y. Suzuki, T. Yamashita, Y. Sugimoto, S. Fujita, and S. Yamaguchi: *ISIJ Int.*, 2009, vol. 49, pp. 564–73.
17. R. Khondker, A. Mertens, and J.R. McDermid: *Mater. Sci. Eng., A*, 2007, vol. 463, pp. 157–65.
18. E.M. Bellhouse and J.R. McDermid: *Mater. Sci. Eng. A*, 2008, vol. 491, pp. 39–46.
19. R. Kavitha and J.R. McDermid: *Surf. Coat. Technol.*, 2012, vol. 212, pp. 152–58.
20. K.M.H. Bhadron: Effect of Starting Microstructure and CGL Compatible Thermal Processing Cycle on the Mechanical Properties of a Medium Mn Third Generation Advanced High Strength Steel. M.A.Sc. Thesis, McMaster University, Hamilton, Canada, 2017.
21. M. Pourmajidian and J.R. McDermid: The 10th International Conference on Zinc and Zinc Alloy Coated Steel Sheet (Galvatech 2015), 2015, pp. 754–61.
22. S. Alibeigi, R. Kavitha, R.J. Meguerian, and J.R. McDermid: *Acta Mater.*, 2011, vol. 59, pp. 3537–49.
23. R. Sagl, A. Jarosik, D. Stifter, and G. Angeli: *Corros. Sci.*, 2013, vol. 70, pp. 268–75.
24. K.M.H. Bhadron, J.R. McDermid and F.E. Goodwin: The 10th International Conference on Zinc and Zinc Alloy Coated Steel Sheet (Galvatech 2015), 2015, pp. 936–43.
25. Morris: *FREED Thermodynamic Database*, v7.8.1, 2013.
26. E.M. Bellhouse and J.R. McDermid: *Metall. Mater. Trans. A*, 2011, vol. 42A, pp. 2753–68.

27. B.R. Strohmaier and D.M. Hercules: *J. Phys. Chem.*, 1984, vol. 88, pp. 4922–29.
28. M.C. Biesinger, B.P. Payne, A.P. Grosvenor, L.W.M. Lau, A.R. Gerson, and R.St.C. Smart: *Appl. Surf. Sci.*, 2011, vol. 257, pp. 2717–30.
29. A. Aoki: *Jpn. J. Appl. Phys.*, 1976, vol. 15, pp. 305–11.
30. N. Birks, G.H. Meier, and F.S. Pettit: *Introduction to the High-temperature Oxidation of Metals*, Cambridge University Press, Cambridge, 2006, p. 338.
31. S. Swaminathan and M. Spiegel: *Appl. Surf. Sci.*, 2007, vol. 253, pp. 4607–19.
32. Y.F. Gong, H.S. Kim, and B.C. De Cooman: *ISIJ Int.*, 2009, vol. 49, pp. 557–63.
33. I.B. Timokhina, P.D. Hodgson, S.P. Ringer, R.K. Zheng, and E.V. Pereloma: *Scripta Mater.*, 2007, vol. 56, pp. 601–04.
34. M. Auinger, V.G. Praig, B. Linder, and H. Danninger: *Corros. Sci.*, 2015, vol. 96, pp. 133–43.
35. E.M. Bellhouse and J.R. McDermid: *Metall. Mater. Trans. A*, 2010, vol. 41A, pp. 1539–53.
36. Y.F. Gong, H.S. Kim, and B.C. De Cooman: *ISIJ Int.*, 2008, vol. 48, pp. 1745–51.
37. K. Kimoto, T. Sekiguchi, and T. Aoyama: *J. Electron Microsc.*, 1997, vol. 46, pp. 369–74.
38. Gatan, <http://www.eels.info/atlas/silicon>. Accessed 12 June 2017.
39. A.P. Grosvenor, E.M. Bellhouse, A. Korinek, M. Bugnet, and J.R. McDermid: *Appl. Surf. Sci.*, 2016, vol. 379, pp. 242–48.
40. J.H. Rask, B.A. Miner, and P.R. Buseck: *Ultramicroscopy*, 1987, vol. 21, pp. 321–26.
41. P.L. Potapov, K. Jorissen, and D. Schryvers: *Phys. Rev.*, 2004, vol. 70, p. 045106.
42. H.K. Schmid and W. Mader: *Micron*, 2006, vol. 37, pp. 426–32.
43. H. Tan, J. Verbeeck, A. Abakumov, and G. Van Tendeloo: *Ultramicroscopy*, 2012, vol. 116, pp. 24–33.
44. J.H. Swisher and E.T. Turkdogan: *Trans. Metall. Soc. AIME*, 1967, vol. 239, pp. 426–31.
45. J. Takada, K. Kashiwagi, and M. Adachi: *J. Mater. Sci.*, 1984, vol. 19, pp. 3451–58.
46. S. Sun and M. Pugh: *Mater. Sci. Eng., A*, 2000, vol. 276, pp. 167–74.
47. J.M. Maigne, M. Lamberigts, and V. Leroy: TMS Fall Meeting, 1991, pp. 21–23.
48. R.C. Weast: *CRC Handbook of Chemistry and Physics*, 64th ed., CRC Press Inc, West Palm Beach, USA, 1978, pp. B200–B16.
49. D.R. Lide: *CRC Handbook of Chemistry and Physics*, 83rd ed., CRC Press, Inc., Boca Raton, Florida, 2002, p. 12.20.
50. R.A. Rapp: *Corr.*, 1965, vol. 21, pp. 382–01.
51. V.A. Lashgari, G. Zimbitas, C. Kwakernaak, and W.G. Sloof: *Oxid. Metal.*, 2014, vol. 82, pp. 249–69.
52. J.M. Maigne, M. Lamberigts, and V. Leroy: *Minerals, Metals & Materials Society*, Warrendale, PA, USA, 1992, pp. 512–28.
53. P. Kofstad: *High Temperature Corrosion*, Elsevier Science Publishers LTD, England, 1988.
54. X.S. Li, S.I. Baek, C.S. Oh, S.J. Kim, and Y.W. Kim: *Scripta Mater.*, 2007, vol. 57, pp. 113–16.
55. D. Huin, P. Flauder, and J.B. Leblond: *Oxid. Met.*, 2005, vol. 64, pp. 131–67.
56. G. Seyed Mousavi and J.R. McDermid: The 11th International Conference on Zinc and Zinc Alloy Coated Steel Sheet (Galvatech 2017), 2017, pp. 485–92.